International Journal of Plasticity 148 (2022) 103144

Contents lists available at ScienceDirect

International Journal of Plasticity

journal homepage: www.elsevier.com/locate/ijplas

Tensile and compressive plastic deformation behavior of medium-entropy Cr-Co-Ni single crystals from cryogenic to elevated temperatures

Le Li [a], Zhenghao Chen [b], Shogo Kuroiwa [a], Mitsuhiro Ito [a], Kyosuke Kishida [a,b,*], Haruyuki Inui [a,b], Easo P. George [c,d]

[a] Department of Materials Science and Engineering, Kyoto University, Kyoto 606-8501, Japan
[b] Center for Elements Strategy Initiative for Structure Materials (ESISM), Kyoto University, Kyoto 606-8501, Japan
[c] Materials Science and Technology Division, Oak Ridge National Laboratory, Oak Ridge, TN 37831, USA
[d] Materials Science and Engineering Department, University of Tennessee, Knoxville, TN 37996, USA

ARTICLE INFO

Keywords:
High entropy alloys
Single crystals
Mechanical properties
Temperature dependence
Critical shear stress

ABSTRACT

The equiatomic Cr-Co-Ni medium-entropy alloy has the face-centered cubic (FCC) structure. Bulk single crystals of this alloy were grown and tested in tension and compression between 14 K and 1373 K with the loading axis parallel to [$\bar{1}$23]. At room temperature, the critical resolved shear stress (CRSS) for {111}<1$\bar{1}$0> slip is 65 ± 5 MPa and does not exhibit a tension-compression asymmetry. It does, however, increase significantly as the test temperature decreases. A dulling of this temperature dependence occurs below 50 K, which may be due to the inertia effect. When the measured values above 50 K are extrapolated to lower temperatures, a value of 225 MPa is estimated for the CRSS at 0 K. This is larger than that (168 MPa) previously determined for the equiatomic Cr-Mn-Fe-Co-Ni high-entropy alloy using a similar procedure. The stacking fault energy of the present Cr-Co-Ni is estimated to be about 14 mJm^{-2}, which is sufficiently low to account for deformation twinning both at 77 K and room temperature. Twinning at 77 K occurs on conjugate ($\bar{1}\bar{1}$1) planes at an onset shear stress of 482 MPa after primary slip and propagates in the form of Lüders deformation. At room temperature, twinning occurs uniformly throughout the gauge section on primary (111) planes at an onset shear stress of 381 MPa after primary and subsequent conjugate slip. Thin layers with the hexagonal close-packed stacking are observed in association with twinning both at 77 K and room temperature.

1. Introduction

There is considerable interest in high-entropy alloys (HEAs) and medium-entropy alloys (MEAs), an interest that stems at least partly from their special atomic structures and mechanical properties (George et al., 2019,2020; Li et al., 2019a; Miracle and Senkov, 2017). Early investigations focused on what role, if any, configurational entropy played in stabilizing solid solutions at high temperatures (Otto et al., 2013a; Wu et al., 2014a). More recently, chemical short-range order, presumably driven by mixing enthalpy, has been a focus, and attempts have been made to elucidate interesting aspects of atomic structure and potential effects on strength (Ding

* Corresponding author: Department of Materials Science and Engineering, Kyoto University, Kyoto 606-8501, Japan.
E-mail address: kishida.kyosuke.6w@kyoto-u.ac.jp (K. Kishida).

https://doi.org/10.1016/j.ijplas.2021.103144
Received 3 September 2021; Received in revised form 29 October 2021;
Available online 31 October 2021

et al., 2018; Hua et al., 2021; Li et al., 2019b; Tamm et al., 2015; Zhang et al., 2017a, 2020). A striking feature of the mechanical properties of certain HEAs and MEAs, especially those with stable or metastable face-centered cubic (FCC) structures, is excellent combination of high strength and high ductility (Gali and George, 2013; George et al., 2019,2020; Gludovatz et al., 2014, 2016; Li et al., 2016, 2019a; Otto et al., 2013b; Yang et al., 2021). One contribution to high strength appears to be their severely distorted crystal lattice, which has been tackled *via* different theoretical approaches to obtain correlations between the strength of HEAs and MEAs and appropriate parameters that describe the distorted crystal lattices, including mean-square atomic displacement (MSAD) and lattice mismatch strain (Okamoto et al., 2016a; Toda-Caraballo and Rivera-Díaz-del-Castillo, 2015; Varvenne et al., 2017; Zhao and Nieh, 2017). High ductility on the other hand has been attributed to deformation twinning, whose propensity is believed to increase with decreasing stacking fault energy, and deformation-induced phase transformations (Laplanche et al., 2016, 2017; Li et al., 2016; Miao et al., 2017; Niu et al., 2018; Otto et al., 2013b; Slone et al., 2018; Wu et al., 2018; Yang et al., 2021; Zhang et al., 2017b). Together, these results indicate it may be possible to tune lattice distortion and stacking fault energy to attain excellent combination of high strength and high ductility in HEAs and MEAs.

Equiatomic Cr-Co-Ni in the FCC solid-solution state has attracted considerable interest, as it exhibits excellent tensile ductility that increases with decreasing temperature and one of the highest strengths among the quaternary and ternary MEA derivatives of the Cr-Mn-Fe-Co-Ni HEA system (Gludovatz et al., 2016; Okamoto et al., 2016a; Schneider et al., 2020; Wu et al., 2014b). Correspondingly, the MSAD value of Cr-Co-Ni is very large and its high strength is consistent with several different theoretical correlations and predictions (Okamoto et al., 2016a; Toda-Caraballo and Rivera-Díaz-del-Castillo, 2015; Varvenne et al., 2017; Zhao and Nieh, 2017). The excellent tensile ductility of Cr-Co-Ni is related to its low stacking-fault energy that results in high propensity for deformation twinning and, in turn, twinning-induced plasticity (TWIP) (Laplanche et al., 2017; Miao et al., 2017; Slone et al., 2018). Thin HCP layers have been observed next to deformation twins in the Cr-Co-Ni MEA suggesting that, in addition to TWIP, TRIP (transformation induced plasticity) may also contribute to its excellent tensile ductility as in high-Mn steels and in certain off-equiatomic HEAs (Bahramyan et al., 2020; De Cooman et al., 2018; Grässel et al., 2000; Li et al., 2016; Li and Raabe, 2017; Lu et al., 2020; Miao et al., 2017; Slone et al., 2018). The theoretically calculated stacking fault energy of the equiatomic Cr-Co-Ni MEA decreases with decrease in temperature, which is *qualitatively* consistent with its experimentally observed increased propensity for twinning and higher tensile ductility at lower temperatures (Laplanche et al., 2017; Zhang et al., 2017b, 2017c; Zhao et al., 2017). Notwithstanding this, it is very difficult to *quantitatively* compare experimental and theoretical results, as most of the former (including CRSS and twinning stress) are deduced from experiments on polycrystals which usually suffer from grain-size effects.

To our knowledge, there are only three studies that used single crystals to investigate the plastic and elastic behavior of equiatomic Cr-Co-Ni (Abuzaid and Patriarca, 2020; Laplanche et al., 2020; Uzer et al., 2018). In these studies, the CRSS for $\{111\}\langle 1\bar{1}0\rangle$ slip was determined to be 69–78 and 140–160 MPa, respectively at room temperature and 77 K, which are considerably lower than those (117 and 183 MPa) estimated from the polycrystalline yield stresses and the corresponding Taylor factor. The twinning shear stress at room temperature was determined to be 78 ± 5 MPa (comparable to the CRSS for $\{111\}\langle 1\bar{1}0\rangle$ slip), which is again much smaller than that (260 ± 30 MPa) estimated from polycrystals (Laplanche et al., 2017). Although the single-crystal data are truly free from grain size effects, the discrepancy with the polycrystalline data seems rather large to be ascribed only to grain size effects. Therefore, additional work with single crystals is needed to deepen our understanding of the mechanical behavior of the equiatomic Cr-Co-Ni MEA.

In the present study, we investigate the plastic deformation behavior of single crystals of the equiatomic Cr-Co-Ni MEA both in tension and in compression as a function of temperature over a wide range, 14–1373 K, in order to experimentally deduce materials parameters (such as CRSS for slip, twinning shear stress as well as stacking fault energy). The results are compared with theoretical estimates.

2. Material and methods

Rods of the equiatomic Cr-Co-Ni MEA were prepared from high-purity (>99.9%) Cr, Co and Ni by arc-melting in Ar. Single crystals were grown from the polycrystalline rods with an optical floating-zone furnace in flowing Ar at a growth rate of 10 mm/h. They were then heat-treated at 1473 K for 168 h, followed by water quenching to suppress, as much as possible, the chemical short-range ordering (SRO) that is expected to develop more significantly at lower temperatures (Ding et al., 2018; Li et al., 2019b; Tamm et al., 2015; Zhang et al., 2017a, 2020). Crystallographic orientations of the heat-treated single crystals were determined by the X-ray back reflection Laue method. Oriented specimens with gauge dimensions of $2 \times 2 \times 5$ mm^3 were prepared by electrical discharge machining for tension and compression. Specimen surfaces were first polished mechanically and then electrolytically in a solution of nitric acid and methanol (1:4 by volume) prior to mechanical testing.

Compression and tensile tests were conducted along the $[\bar{1}23]$ loading axis on an Instron-type testing machine in vacuum in the temperature range 14–1373 K at an initial strain rate of 1×10^{-4} s^{-1}. Details of the tensile tests are described in the supplementary materials to this paper. The strain-rate sensitivity of flow stress was measured by strain-rate jump tests at selected temperatures below room temperature. Deformation microstructures were examined in an optical microscope (OM) and scanning electron microscope (SEM) equipped with electron back-scatter diffraction (EBSD) and energy dispersive X-ray spectroscopy (EDS) systems. Fine deformation microstructures were examined by transmission electron microscopy (TEM) and scanning transmission electron microscopy (STEM) with JEOL JEM-2000FX, JEM-2100F and JEM-ARM200F electron microscopes. Thin foils for TEM/STEM observations were prepared by electro-polishing in a solution of nitric acid, ethylene glycol and methanol (2:5:20 by volume).

3. Results

3.1. Quality of single crystals

Our as-grown single crystals exhibited a featureless microstructure without significant heterogeneity caused by rapid dendritic growth, because of the slow growth rate employed (10 mm/h) and the high thermal gradient at the solid-liquid interface in the optical floating-zone furnace. The chemical composition determined by wet chemistry averaged over 5 different measurements on single crystals quenched from 1473 K is 33.65Cr – 33.22Co – 33.13Ni (at.%), which is close to the nominal equiatomic composition. EDS mapping in the SEM confirmed that the constituent elements are distributed homogeneously and do not form any secondary phases.

In the selected-area electron diffraction (SAED) pattern taken along the [111] zone axis of a single crystal water-quenched from 1473 K (Fig. 1), some diffuse intensity is observed at positions of 1/3{422} (marked with circles in Fig. 1) in addition to Bragg spots of the FCC structure. This is similar to what has been observed in single crystals of the Cr-Mn-Fe-Co-Ni quinary equiatomic high-entropy alloy (Kawamura et al., 2021; Okamoto et al., 2016b; Zhou et al., 2020), and is indicative of local fluctuation in interatomic distances accompanied by static displacement of the constituent elements due to their atomic radius differences and/or chemical short-range order. Thus, the single crystals of the equiatomic Cr-Co-Ni MEA are true solid solutions with the FCC structure, but the degree of SRO present in our single crystals after quenching from 1473 K cannot be precisely determined from such SAED patterns and requires further investigation considering the fact that the difference in atomic scattering factor among Cr, Co and Ni is virtually negligible and therefore, it is technically impossible to detect any kind of atomic ordering formed with Cr, Co and Ni simply by SAED. The evolution of diffuse intensity at positions of 1/3{422} with annealing and its effects on yield strength are part of a follow-on study that will be described in a subsequent paper.

3.2. Compressive deformation

3.2.1. Stress-strain behavior

Typical compressive stress-strain curves are shown in Fig. 2. All compression tests began at a strain rate of 1×10^{-4} s^{-1} to determine the yield stress. Above room temperature, straining was continued at this rate but, at room temperature and below, strain-rate jump tests were performed within the strain range of 'easy glide' (stage I) to minimize effects of work hardening on the strain-rate sensitivity measurements. At all tested temperatures, only (111)[$\bar{1}$ 01] slip occurred in stage I with no deformation twinning, as confirmed by examination in OM, SEM and TEM. Deformation markings are very straight, in particular at lower temperatures, traversing from one surface to another (examples at 77 K, 212 K and room temperature are shown in Fig. 3) and they gradually cover the gauge section as the plastic strain increases until it is filled with these straight (111) slip lines at the end of stage I, which extends to more than 20% plastic strain at room temperature (as can be seen in the tensile stress-strain curve of Fig. 7, which will be discussed later).

From tests such as those described above, the 0.2% offset yield stress was determined and the Schmid factor of 0.467 was then used to calculate the CRSS for (111)[$\bar{1}$01] slip whose temperature dependence is plotted in Fig. 4. For comparison, our previous results for the quinary equiatomic Cr-Mn-Fe-Co-Ni HEA single crystals (Kawamura et al., 2021) are also shown. The CRSS increases rapidly as the temperature is decreased below room temperature, as observed in many conventional FCC solid-solution alloys and FCC HEAs. However, three characteristic behaviors of the present MEA are worth noting. Firstly, a dulling of the temperature dependence of CRSS below 50 K is observed in equiatomic Cr-Co-Ni, which can be seen more clearly in the magnified view shown in the inset of Fig. 4. While this has long been known to occur in some conventional FCC alloys (such as Cu alloys with Al, Ni or Ge) below 77 K through the so-called dislocation inertia effect (Schwartz et al., 1977), it was not evident in our earlier study of the equiatomic Cr-Mn-Fe-Co-Ni HEA down to 10 K (Kawamura et al., 2021). However, Tirunilai et al. (2020) recently reported a plateau in the yield stress-temperature curve for Cr-Mn-Fe-Co-Ni polycrystals below 15 K. Therefore, more detailed study of the inertia effect in the quinary equiatomic

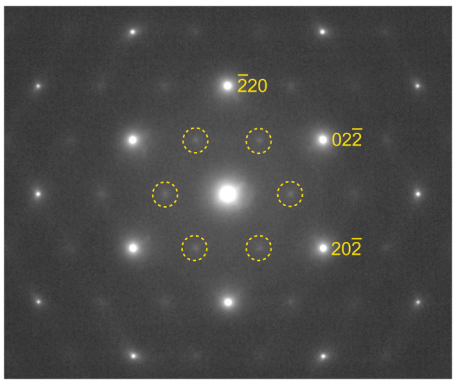

Fig. 1. SAED pattern with the [111] incidence obtained from a single crystal of the equiatomic Cr-Co-Ni MEA annealed at 1473 K for 168 h followed by water quenching. Diffuse intensities at positions of 1/3{422} are marked with circles.

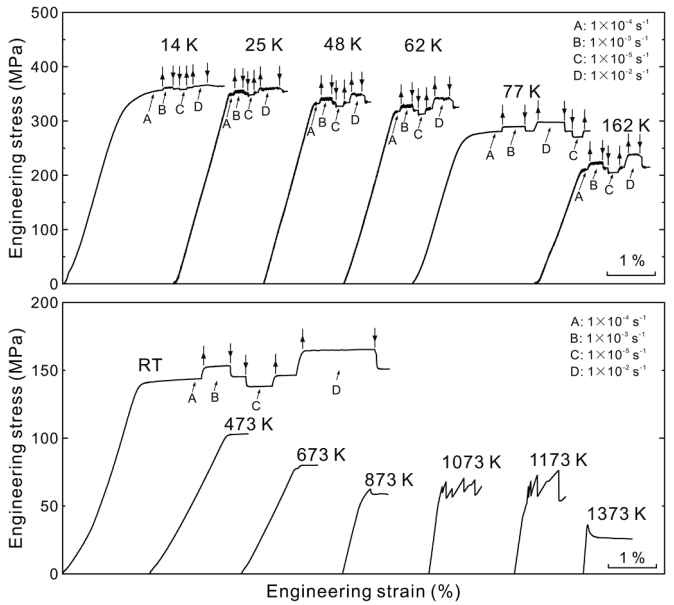

Fig. 2. Stress-strain curves obtained for [$\bar{1}$23]-oriented single crystals deformed in compression. Compression tests were usually started at a strain rate of 1×10^{-4} s^{-1} to determine the yield stress and then strain-rate sensitivity were measured by strain-rate jump tests (at room temperature and below).

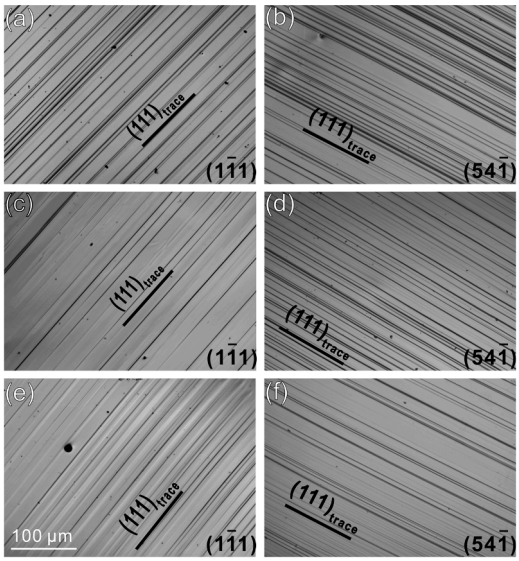

Fig. 3. Deformation markings observed on two orthogonal side surfaces ((a,c,e) (1$\bar{1}$1) and (b,d,f) (54$\bar{1}$)) of [$\bar{1}$23]-oriented single crystals deformed in compression at (a,b) 77 K, (c, d) 212 K and (e, f) room temperature.

Cr-Mn-Fe-Co-Ni HEA is needed. Secondly, an inflection in the CRSS-temperature curve of the equiatomic Cr-Co-Ni MEA is clearly observed at around 473 K. A close look at the temperature dependence of CRSS of the equiatomic Cr-Mn-Fe-Co-Ni HEA suggests a similar inflection may be present in that alloy also, but the paucity of data in the relevant temperature range precludes a definitive assessment. The reason for the inflection is not clear yet, but we suspect it may be related to the motion of quenched-in vacancies from the 1473 K heat treatment because our inflection temperature of 473 K is also the onset temperature for migration of vacancies introduced by electron irradiation in HEAs and MEAs in the Cr-Mn-Fe-Co-Ni system (Sugita et al., 2020). Finally, there is a slight increase of the CRSS of the equiatomic Cr-Co-Ni MEA above 1073 K, where serrated flow is observed in the stress-strain curves (Fig. 2). This was also observed in the equiatomic Cr-Mn-Fe-Co-Ni HEA (Kawamura et al., 2021). Based on the strain-rate and temperature sensitivity of flow stress (including the extent of serration), the serrated flow has been interpreted to be caused by the interaction between solute atoms (which in the case of equiatomic alloys are simply one of the constituent elements) and dislocations (more

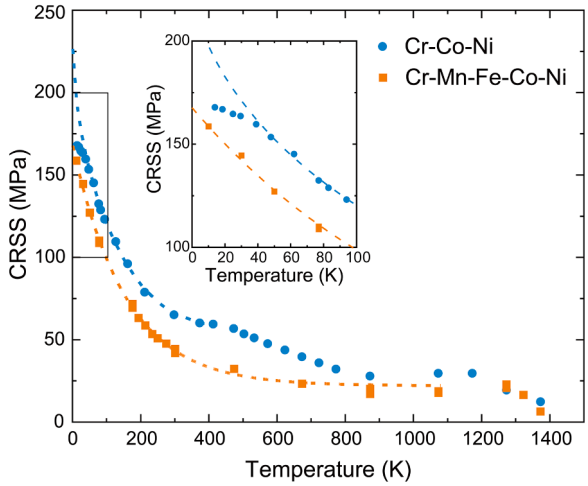

Fig. 4. Temperature dependence of CRSS for (111)[$\bar{1}$01] slip in the equiatomic Cr-Co-Ni MEA. Data for the equiatomic Cr-Mn-Fe-Co-Ni HEA (Kawamura et al., 2021) are shown for comparison.

specifically, extended dislocations bounding a stacking fault), a phenomenon referred to as the Portevin-Le Chatelier (PLC) effect, as discussed in our previous paper on single crystals of the equiatomic Cr-Mn-Fe-Co-Ni HEA (Kawamura et al., 2021) and also in a paper on polycrystals of various MEA and HEA (Tsai et al., 2019).

The CRSSs are considerably higher for the ternary equiatomic Cr-Co-Ni MEA (65 and 130 MPa) than for the quinary equiatomic Cr-Mn-Fe-Co-Ni HEA (44 and 113 MPa) (Kawamura et al., 2021) at room temperature and 77 K, respectively. These CRSS values of the equiatomic Cr-Co-Ni MEA are comparable to that reported by Uzer et al. (2018) at room temperature (69 MPa) but are considerably lower than those reported by Abuzaid and Patriarca (2020) at room temperature (78 MPa) and at 77 K (140–160 MPa). The CRSS value at 0 K for the equiatomic Cr-Co-Ni MEA is estimated to be 225 MPa by extrapolating the CRSS-temperature curve down to 0 K (excluding the data points below 50 K in the anomalous temperature range that are influenced by the inertia effect). The 0 K CRSS value thus estimated is comparable to that (215 MPa) estimated from polycrystals of the equiatomic Cr-Co-Ni MEA (Okamoto et al., 2016a; Wu et al., 2014b). The 0 K CRSS value of the equiatomic Cr-Co-Ni MEA is considerably larger than that (168 MPa) of the equiatomic Cr-Mn-Fe-Co-Ni HEA (Kawamura et al., 2021). This is consistent with experimental data on polycrystals (Wu et al., 2014b) as well as the prediction for the 0 K CRSS from the values of mean-square atom displacement (Okamoto et al., 2016a).

3.2.2. *Strain-rate sensitivity of flow stress*

The strain-rate sensitivity of flow stress in the strain range of easy glide is plotted in Fig. 5(a). In this figure, the plotted shear stress and shear strain were converted from axial stress and strain assuming single (111)[$\bar{1}$01] slip. In stage I, the flow stress at fixed strain rate and temperature does not depend significantly on strain. A clearer view of the extent of the strain-rate sensitivity of flow stress shown in Fig. 5(a) can be obtained by evaluating its gradient as a function of temperature, which is shown in Fig. 5(b). Since the flow stress of the equiatomic Cr-Co-Ni MEA increases with strain rate, the strain-rate sensitivity of flow stress increases with decreasing temperature down to 62 K (because of the more significant temperature dependence of CRSS), below which the strain-rate sensitivity of flow stress becomes smaller as the temperature is decreased as shown in Fig. 5(b). The decrease observed below 62 K is clear evidence for the inertia effect (Schwartz et al., 1977), which is responsible for the duller temperature dependence of CRSS (Fig. 4).

Fig. 5(c) plots the temperature dependence of the activation volume (V) estimated using the following conventional equation:

$$V = kT\left[\frac{\partial \ln \dot{\gamma}}{\partial \tau}\right]_T \tag{1}$$

where k is the Boltzmann constant, T is the absolute temperature, $\dot{\gamma}$ is the shear strain rate sensitivity of flow stress, and τ is the shear stress. For comparison, values of the activation volume similarly determined for single crystals of the equiatomic Cr-Mn-Fe-Co-Ni HEA (Kawamura et al., 2021) are also plotted in Fig. 5(c). The activation volume of the equiatomic Cr-Co-Ni MEA is less temperature dependent than that of the equiatomic Cr-Mn-Fe-Co-Ni HEA. Additionally, while the activation volume at room temperature is much smaller for Cr-Co-Ni (~130 b^3) than for Cr-Mn-Fe-Co-Ni (~233 b^3), it is inverse at 14 K (~34 b^3 for the Cr-Co-Ni and ~5 b^3 for Cr-Mn-Fe-Co-Ni). Of interest to note in Fig. 5(c) is that the activation volume of the Cr-Co-Ni MEA increases slightly with decreasing temperature below 50 K, which is consistent with the inertia effect occurring in that temperature range. The activation volumes at 77 K and room temperature (~36 and ~130 b^3, respectively) obtained for Cr-Co-Ni in the present study are considerably larger than those (~14 and ~47 b^3) reported for polycrystals of the same alloy by Wu et al. (2016). The reason for the discrepancy remains to be clarified.

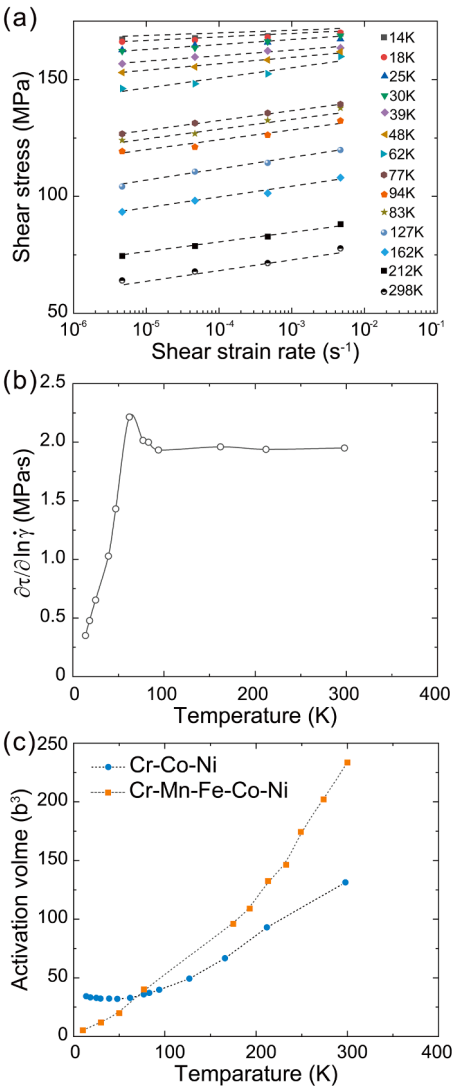

Fig. 5. (a) The strain-rate sensitivity of flow stress measured for [$\bar{1}$23]-oriented single crystals of the equiatomic Cr-Co-Ni MEA. (b) The gradient of the strain-rate sensitivity shown in (a) plotted as a function of temperature. (c) Temperature dependence of activation volume for deformation in the equiatomic Cr-Co-Ni MEA, together with data for the equiatomic Cr-Mn-Fe-Co-Ni HEA (Kawamura et al., 2021) for comparison.

3.2.3. Dislocation structures

A typical dislocation structure observed after room-temperature compression to about 3% plastic strain is shown in Fig. 6(a). Planar arrays of dislocations were observed in the TEM foil extracted parallel to the (111) primary slip plane; no cell structures were observed. These observations are consistent with the alloy being a single crystal as well as its low stacking fault energy. Widely dissociated, coupled partial-dislocations were clearly visible in weak-beam TEM images (see example in Fig. 6(b)). From the separation distances measured as a function of angle (θ) between the Burgers vector and line direction of dislocations, the stacking fault energy is 14 ± 3 mJ/m^2 (Fig. 6(c)). Scatter in dissociation widths at a given θ in the present equiatomic Cr-Co-Ni MEA is similar in magnitude to those in pure metals such as pure Cu and Ag (Cockayne et al., 1971; Stobbs and Sworn, 1971) and in the equiatomic Cr-Mn-Fe-Co-Ni HEA (Kawamura et al., 2021; Okamoto et al., 2016a). No significant local variation in dissociation widths was observed in the present equiatomic Cr-Co-Ni MEA, in contrast to what has been reported elsewhere (Slone et al., 2018; Smith et al., 2016). The value of stacking fault energy (14 ± 3 mJ/m^2) obtained in the present study of equiatomic Cr-Co-Ni is considerably smaller than that (30 mJ/m^2) obtained previously for equiatomic Cr-Mn-Fe-Co-Ni (Kawamura et al., 2021; Okamoto et al., 2016a), is also a bit smaller than those determined from polycrystals of equiatomic Cr-Co-Ni (22 ± 4 mJ/m^2 in (Laplanche et al., 2017) and 18 ± 4 mJ/m^2 in Liu et al., 2018) and is in good agreement with that (10–20 mJ/m^2) obtained for polycrystalline Cr-Co-Ni (Shih et al., 2021). Of interest to note is that a very low stacking fault energy of 8.18 ± 1.43 mJ/m^2 has been reported by Zhang et al. (2020) for a specimen quenched from 1473 K, which is exactly the same quenching procedure employed in the present study. In their paper, Zhang et al. (2020) also mentioned that the stacking fault energy of the equiatomic Cr-Co-Ni alloy increases when annealed at lower temperatures

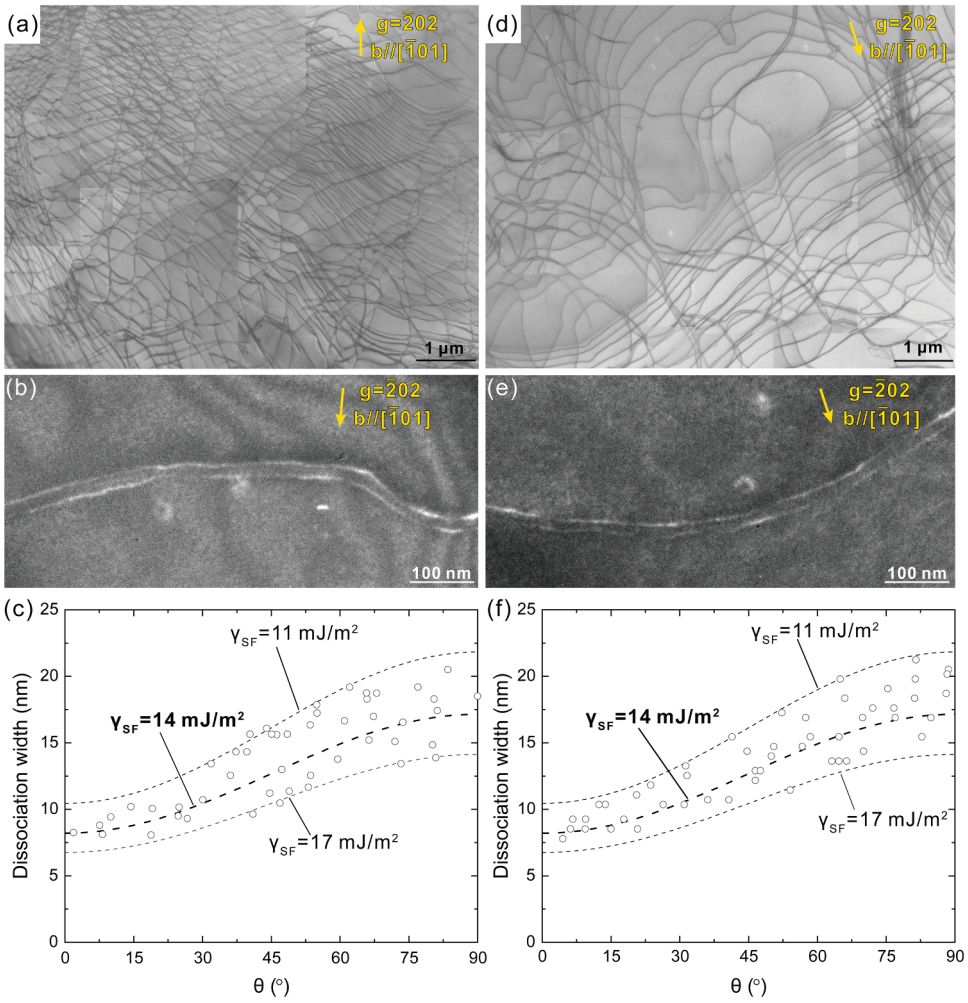

Fig. 6. Typical dislocation structures observed in a [$\bar{1}$23]-oriented single crystal of the equiatomic Cr-Co-Ni MEA deformed in compression to about 3% plastic strain at (a) room temperature and (d) 77 K. Weak-beam image of a widely separated partial dislocations in specimens deformed at (b) room temperature and (e) 77 K. Dissociation widths of partials plotted as a function of angle between the Burgers vector of 1/2[$\bar{1}$01] and dislocation line are shown in (c) and (f) for room temperature and 77 K, respectively.

accompanied by an increase in the extent of short-range ordering.

Typical dislocation structure observed at room temperature in a TEM foil extracted parallel to the (111) primary slip plane of a bulk specimen pre-compressed at 77 K to about 3% plastic strain is shown in Fig. 6(d). Dislocation arrays are again very planar without the formation of dislocation cells. Consistent with this, dislocations are observed clearly to dissociate into two Shockley partials (Fig. 6(e)). Stacking fault energies were estimated from the dislocation dissociation widths, as described above, to evaluate the temperature dependence of stacking fault energy and compare with theoretical calculations (Zhang et al., 2017b, 2017c; Zhao et al., 2017). However, the estimated stacking fault energy for the specimen deformed at 77 K is 14 ± 3 mJ/m^2 (Fig. 6(f)), which is virtually the same as that obtained from the specimen deformed at room temperature (Fig. 6(c)). This suggests that, regardless of the deformation temperature, the dislocation dissociation width settles at the room-temperature equilibrium value as long as TEM observations are made at room temperature. *In-situ* measurements of the dissociation width are therefore needed to explore the temperature dependent stacking fault energy of the equiatomic Cr-Co-Ni MEA.

3.3. Tensile deformation

3.3.1. Stress-strain behavior

Stress-strain curves of the Cr-Co-Ni single crystals tested a constant engineering strain rate of 1×10^{-4} s^{-1} at room temperature and 77 K are shown in Fig. 7(a). Stage I (strain range of easy glide) is considerably longer for the ternary equiatomic Cr-Co-Ni MEA than for the quinary equiatomic Cr-Mn-Fe-Co-Ni HEA both at room temperature and 77 K, consistent with the considerably lower stacking fault energy of the former.

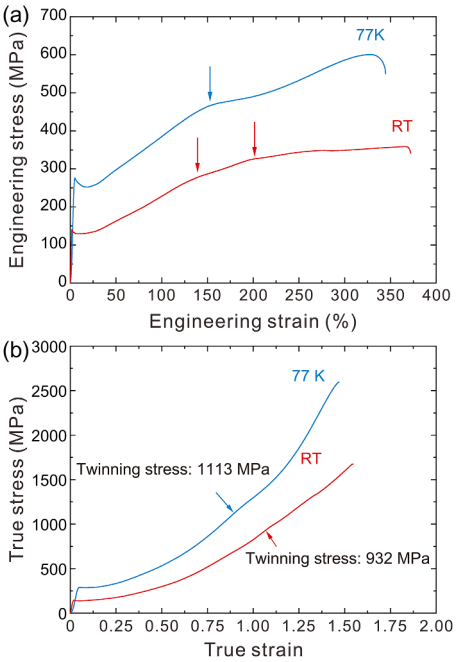

Fig. 7. (a) Engineering stress-engineering strain curves and (b) true stress-true strain curves obtained for [$\bar{1}$23]-oriented single crystals of the equiatomic Cr-Co-Ni MEA deformed in tension to failure at 77 K and room temperature.

At room temperature, stage I extends to about 25% plastic strain, which is much larger than the 13% strain of the Cr-Mn-Fe-Co-Ni HEA (Kawamura et al., 2021). This is consistent with the general belief that stage I is longer in FCC alloys with lower stacking fault energy (Haasen, 1996). The long stage I is followed by stage II with a high work-hardening rate of about $G/390$ (G: shear modulus), which is well within the range of many conventional FCC alloys. Similar to what is observed in stage I, plastic deformation in Stage II also occurs essentially by (111)[$\bar{1}$01] primary slip, although deformation markings corresponding to the ($\bar{1}\bar{1}$1)[011] conjugate slip system are also sporadically observed. The room-temperature CRSS in tension is 62 MPa, which agrees well with that (65 $\pm$ 5 MPa) obtained in compression at room temperature (see earlier section). These results confirm the lack of any significant tension-compression asymmetry in yield stress, which implies 'normal' behavior of dislocations. Interestingly, stage II is followed by a large region of flow accompanied by two inflection points (red arrows) before failure eventually occurs. This is in contrast to the room-temperature tensile deformation behavior of single crystals of the quinary equiatomic Cr-Mn-Fe-Co-Ni HEA, in which failure occurs at the end of stage II (Kawamura et al., 2021).

To identify physical origins of the two inflection points in the stress-strain curves, a room-temperature tensile test was interrupted repeatedly at points A–E in Fig. 8(a) so that the evolution of microstructure could be examined by OM (Fig. 8(b)) and SEM with EBSD (Fig. 8(c)). The first inflection point, marked by the arrow between points B and C in Fig. 8(a) and corresponding to a sudden change in work-hardening rate at a strain of about 140%, was confirmed to be due to the change of the dominant slip system from the (111)[$\bar{1}$01] primary slip system to the ($\bar{1}\bar{1}$1)[011] conjugate slip system. Therefore, the first inflection point corresponds to the end of overshoot of the rotation of the tensile axis toward [$\bar{1}$01]. The tensile-axis orientation at this point was determined to be [$\bar{5}$49] (Fig. 8(d)). After the first inflection point, ($\bar{1}\bar{1}$1)[011] conjugate slip occurs in the form of Lüders band, as seen in the low- magnification SEM/EBSD image corresponding to point C, Figs. 8(c) and S2 of the supplementary materials. The Lüders front propagates from the top of the gauge section to the bottom until the whole gauge section is fully covered with deformation markings of the conjugate slip at the second inflection point (marked by arrow between points D and E in Fig. 8(a)). In the quinary equiatomic Cr-Mn-Fe-Co-Ni HEA with the [$\bar{1}$23] orientation, conjugate twinning is observed to occur at 77 K in the form of Lüders band after stage II dominated by primary slip (Kawamura et al., 2021). Although the Lüders band appears similarly on the conjugate system in equiatomic Cr-Co-Ni at room temperature, twinning is not involved in the deformation after the first inflection point, as is evident from Fig. 8(c) which shows SEM/EBSD images at points C and D (prior to the second inflection point). The orientation difference of 60° between the matrix and twin is clear in Fig. 8(e) for the E3 region of the SEM/EBSD image in Fig. 8(c). The second inflection point at a strain of about 200% after point D was confirmed to correspond to the change of the dominant deformation mode from ($\bar{1}\bar{1}$1)[011] conjugate slip to (111)[$\bar{2}$11] primary twinning, as clearly seen in the SEM/EBSD images of point E in Fig. 8(c). The second inflection point corresponds to the end of overshoot of the tensile axis back toward [011] in the original standard triangle by the conjugate slip system; the tensile-axis orientation at this point was determined to be [$\bar{9}$ 10 19] (Fig. 8(d)). Primary twinning after the second inflection point occurs uniformly throughout the whole gauge length (SEM/EBSD images of E1-E3 of Fig. 8(c)) rather than in the form of Lüders band as in the case of conjugate twinning in the quinary equiatomic Cr-Mn-Fe-Co-Ni HEA at 77 K (Kawamura et al., 2021). Of interest to note in Fig. 8(a) is

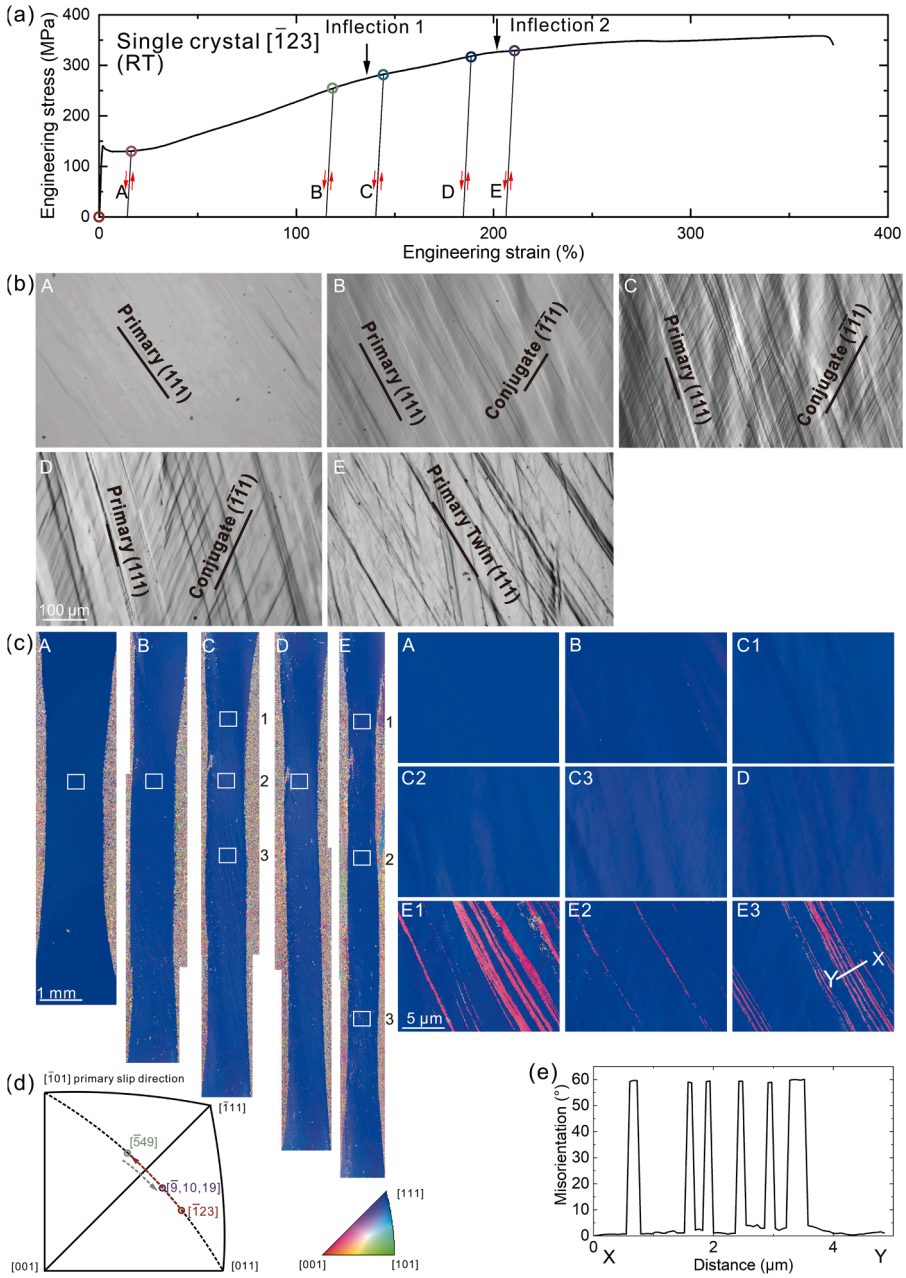

Fig. 8. (a) Stress-strain curve of a [1̄23]-oriented single crystal of the equiatomic Cr-Co-Ni MEA deformed in tension at room temperature, showing the points A-E at which the test was interrupted for microstructure observations. (b) Microstructures observed by optical microscopy at points A–E on the (1$\bar{1}$1) surface. (c) EBSD orientation maps at points A–E with the framed areas shown enlarged on the right-hand side. (d) Tensile-axis rotation during deformation shown in the stereographic projection. (e) Misorientation along the line *X* - *Y* in the EBSD map of E3, showing the existence of deformation twins.

that strain to failure at room temperature is significantly higher for equiatomic Cr-Co-Ni (370%) than for equiatomic Cr-Mn-Fe-Co-Ni (110%) (Kawamura et al., 2021). In view of the fact that twinning does not occur in the latter at room temperature (Kawamura et al., 2021), the activation of twinning in the former seems to be responsible for its enhanced room-temperature tensile ductility.

At 77 K, the CRSS in tension increases significantly to 131 MPa, from 65 MPa at room temperature. The CRSS at 77 K coincides well with that (133 ± 6 MPa) obtained in compression at 77 K (see earlier section), confirming once again the absence of any significant tension-compression asymmetry in yield stress. The CRSS value at 77 K obtained in the present study is somewhat lower than that (140–160 MPa) obtained in tension by Abuzaid and Patriarca (2020). Stage I (easy glide) with low work-hardening rate occurs up to more than 22% plastic strain, which is larger than that (17%) of the equiatomic Cr-Mn-Fe-Co-Ni HEA at 77 K (Kawamura et al., 2021).

The work-hardening rate for Stage II at 77 K is $G/344$, which is similar to the value at room temperature.

There is an inflection point in the 77 K tensile stress-strain curve after a large plastic strain of about 150% in stage II. This inflection point was confirmed to correspond to the onset of deformation twinning through repeated microstructure observations during interrupted tests, as shown in Fig. 9 and corresponding to points A–C in Fig. 9(a). Deformation microstructures examined by OM and SEM with EBSD are summarized in Fig. 9(b) and 9(c), respectively. The (111)[$\bar{1}$01] primary slip system dominates during stage I and stage II with the ($\bar{1}\bar{1}$1)[011] conjugate slip system occurring only sporadically up to the inflection point at a strain of about 150%. No evidence for deformation twinning is detected up to point B. Beyond the inflection point, deformation markings of twinning on the conjugate plane can be seen, as shown in the SEM/EBSD images of point C in Fig. 9(c). The orientation difference of 60° between the

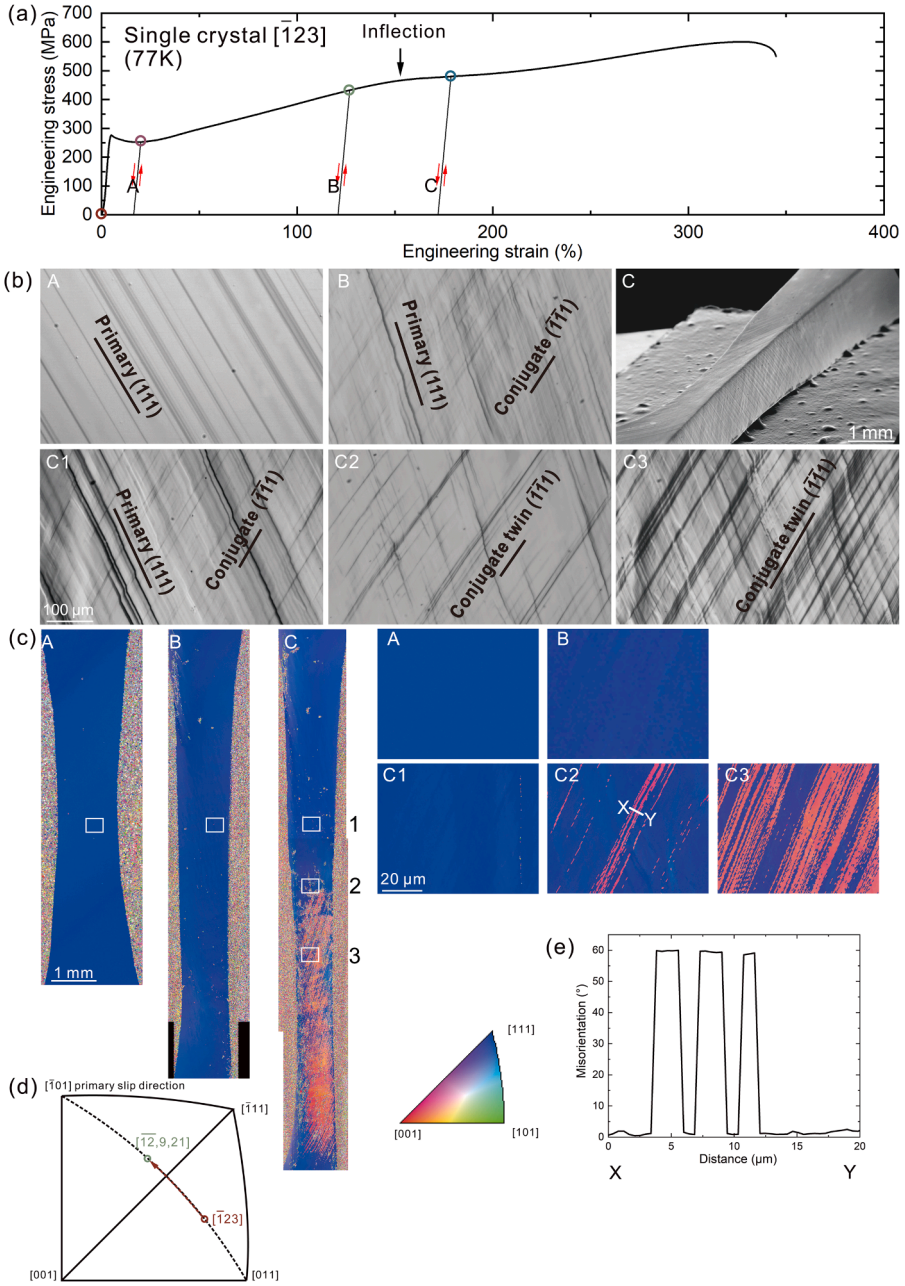

Fig. 9. (a) Stress-strain curve of a [$\bar{1}$23]-oriented single crystal of the equiatomic Cr-Co-Ni MEA deformed in tension at 77 K, showing the points A–C at which the test was interrupted for microstructure observations. (b) Microstructures observed by optical microscopy at points A–C on the (1$\bar{1}$1) surface. (c) EBSD orientation maps at points A–C with the framed areas shown enlarged on the right-hand side. (d) Tensile-axis rotation during deformation shown in the stereographic projection. (e) Misorientation along the line *X* - *Y* in the EBSD map of C2, showing the existence of deformation twins.

matrix and twin is clearly detected in Fig. 9(e) for the C2 region of the SEM/EBSD image in Fig. 9(c). As seen in the low-magnification SEM/EBSD images of point C, Fig. 9(c), conjugate twinning after the inflection point occurs in the form of Lüders band with its front propagating from the bottom of the gauge section to the top until the whole gauge section is covered with the deformation markings of the conjugate twinning. The inflection point at a strain of about 150% was thus confirmed to correspond to the change of the dominant deformation mode from (111)[$\bar{1}$01] primary slip to ($\bar{1}\bar{1}$1)[$\bar{1}$21] conjugate twinning. This is exactly the same as what was previously observed in similarly oriented single crystals of the quinary equiatomic Cr-Mn-Fe-Co-Ni HEA tested at 77 K (Kawamura et al., 2021). Thus, the inflection point corresponds to the end of overshoot of the tensile axis toward [$\bar{1}$01]. The tensile-axis orientation at this point was determined to be [$\bar{1}\bar{2}$ 9 21] (Fig. 9(d)). The extent of overshoot of the tensile axis is larger at 77 K (4.7°) than at room temperature (3.7°) for the ternary equiatomic Cr-Co-Ni MEA and also larger than that for the quinary equiatomic Cr-Mn-Fe-Co-Ni HEA at 77 K (3.7°) (Kawamura et al., 2021). All these observations are consistent with the general belief that the extent of overshoot of the tensile axis is larger for materials with lower stacking fault energies. Of interest to note in Fig. 7(a) is that the tensile elongation to failure of equiatomic Cr-Co-Ni is larger at room temperature than at 77 K. While this may be related to the lower strength at room temperature compared to that at 77 K combined with the occurrence of deformation twinning at both temperatures in Cr-Co-Ni, it is opposite to what is observed not only for polycrystals of the equiatomic Cr-Co-Ni MEA (Laplanche et al., 2017; Wu et al., 2014b) but also for [$\bar{1}$23]-oriented single crystals of the equiatomic Cr-Mn-Fe-Co-Ni HEA (Kawamura et al., 2021).

Tensile true stress-true strain curves at room temperature and 77 K were obtained from the engineering stress-engineering strain curves (Fig. 7(a)) using standard equations assuming uniform plastic deformation for the entire stage as a first approximation and are shown in Fig. 7(b) (Kawamura et al., 2021). This was done to deduce the twinning shear stress for the equiatomic Cr-Co-Ni MEA at room temperature and 77 K, by properly taking into account the considerably reduced cross-section of the specimen when deformation twinning commences after a large amount of plastic strain. Although the Lüders deformation by the conjugate slip was observed at room temperature, the true stress value for the onset of deformation twinning at room temperature is not considered to be affected much by the non-uniform variation of cross section because the Lüders band was confirmed to sweep over the entire gauge section in prior to the second inflection point corresponding to the onset of deformation twinning. The true stress for onset of deformation twinning at room temperature is determined to be 932 MPa (Fig. S3(a,c) of the supplementary materials), which can be converted into a twinning shear stress of 381 MPa with the Schmid factor (0.409) for (111)[$\bar{2}$11] primary twinning at the [$\bar{9}$ 10 19] tensile-axis orientation. The above twinning shear stress is considerably larger than the previously reported value (78 ± 5 MPa for [110]-, [111]- and [123]-oriented single crystals of equiatomic Cr-Co-Ni) by Uzer et al. (2018). They claimed that nano-twinning was observed at 4% strain for [110]-oriented crystals and at 10% strain for [123]-oriented crystals in tension at room temperature. However, these strain levels are well within stage I where single glide of the primary slip system dominates. Similarly, the twinning shear stress of 482 MPa is obtained from the onset true stress for deformation twinning at 77 K (1113 MPa, Fig. S3(b,d) of the supplementary materials) and the Schmid factor (0.433) for ($\bar{1}\bar{1}$1)[$\bar{1}$21] conjugate twinning at the [$\bar{1}\bar{2}$ 9 21] orientation. The twinning shear stresses obtained at room temperature and 77 K are both considerably higher than that (291 MPa) theoretically estimated by Huang et al. (2018). The twinning shear stress increases significantly from 381 MPa at room temperature to 482 MPa at 77 K. This contrasts with the general belief that twinning is stress-controlled in many FCC alloys making the twinning stress almost temperature-independent (Christian and Mahajan, 1995). We will discuss this later in detail in Section 4.2.

Side and top views of our single-crystal fracture surfaces after failure at room temperature and 77 K are shown respectively in Fig. 10(a), (b) and . 10(c), (d). The specimens exhibit apparent necking behavior and the dimple-type fracture surfaces typical for ductile failure at both temperatures.

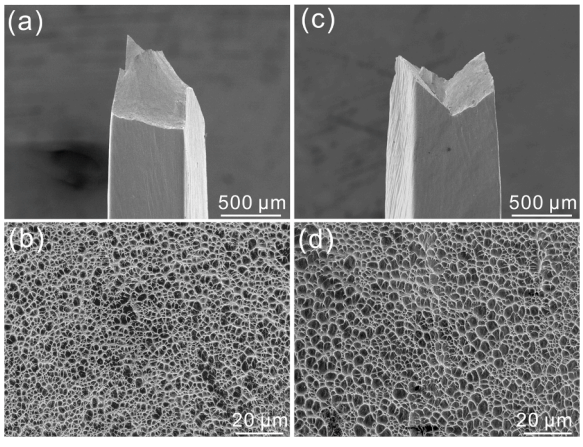

Fig. 10. (a,c) Side and (b,d) top views of fracture surfaces in [$\bar{1}$23]-oriented single crystals of the equiatomic Cr-Co-Ni MEA deformed in tension at (a,c) room temperature and (b, d) 77 K.

3.3.2. Deformation fine microstructures

Evolution of deformation fine microstructures during deformation twinning in [$\bar{1}$23]-oriented single crystals of the equiatomic Cr-Co-Ni MEA at room temperature and 77 K were investigated by TEM/STEM observations with thin foils cut perpendicular to the twinning plane. The thickness and volume fraction of twins (and HCP layers, if present) were investigated by taking TEM dark-field (DF) images with the objective aperture set to the position of a reflection of the {111}-type of the twin for single crystals deformed to 205% strain (after the second inflection point), to failure at room temperature, and to failure at 77 K, as shown in Fig. 11(a), (c) and (e), respectively.

Since deformation twinning occurs uniformly on the (111) primary plane at room temperature, evolution of fine microstructures during deformation twinning can be investigated as a function of plastic strain at room temperature. As seen in the SAED pattern of the inset of Fig. 11(a), in addition to Bragg reflection spots of the matrix and twin, streaks are observed to run parallel to the (111) primary plane normal, indicating that thin twins are formed randomly. No significant difference is noticed in the SAED pattern of the inset of Fig. 11(c) when the strain level is increased to failure. However, both thickness and volume fraction of twins in the corresponding DF images increase considerably as the strain level is increased, as shown in the histograms of twin thickness distributions of Fig. 11(b) and (d). While the average twin thickness and twin volume fraction are estimated respectively to be 4.6 nm and 2.9% in the early stage of deformation twinning, they both increase respectively to 14.9 nm and 10.3% at failure. This may indicate that when deformation twinning occurs uniformly, twin thickening plays an important role in increasing the twin volume fraction as the strain level increases

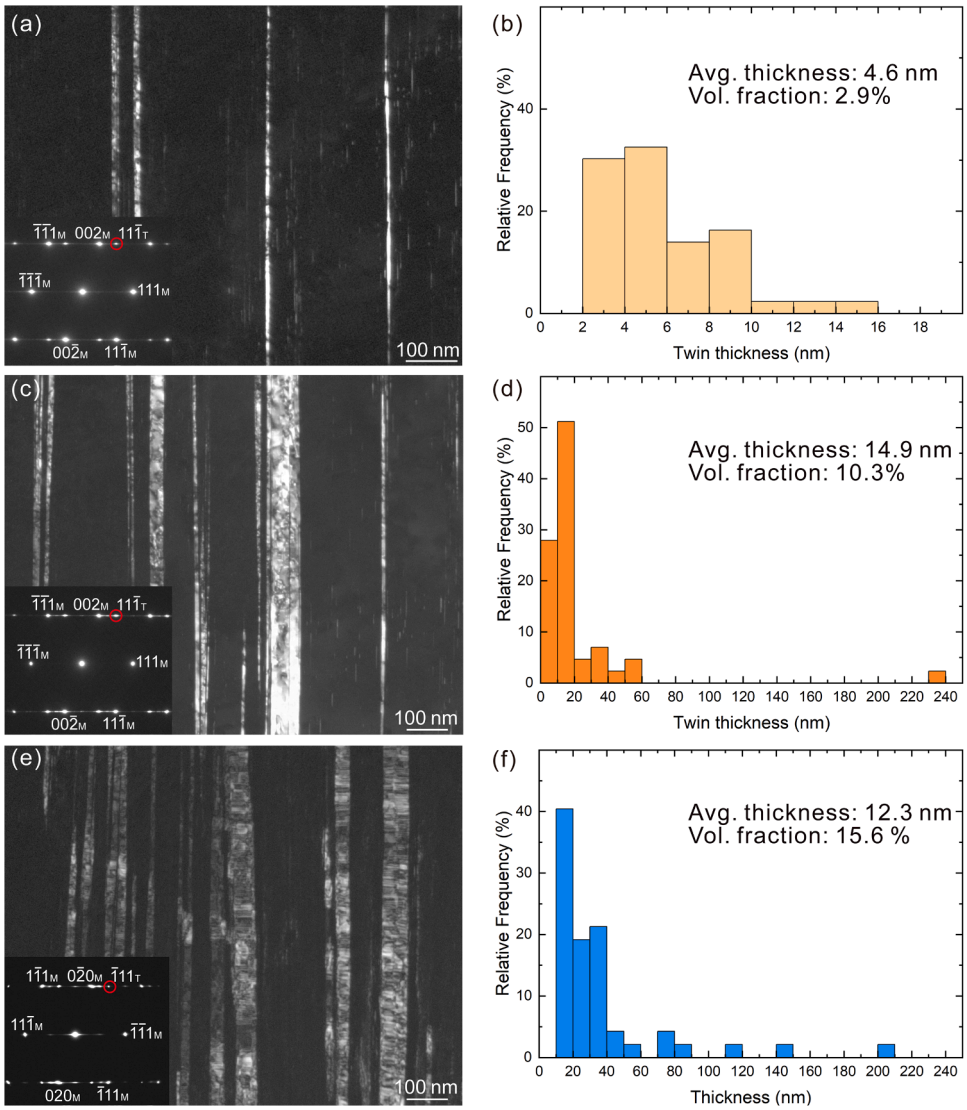

Fig. 11. Deformation twins viewed end-on by dark-filed TEM imaging in [$\bar{1}$23]-oriented single crystals of the equiatomic Cr-Co-Ni MEA deformed in tension to different strains: (a) slightly beyond the inflection point, (c) to failure at room temperature and (e) to failure at 77 K. Twin thickness distributions for (a), (c) and (e) are shown in (b), (d) and (f), respectively.

in single crystals of the Cr-Co-Ni ternary equiatomic MEA.

At 77 K, on the other hand, deformation twinning occurs in the form of Lüders band in the equiatomic Cr-Co-Ni MEA so that localized deformation occurs only in the Lüders front that sweeps from one end of the gauge section to the other. Because of this, only a single crystal deformed to failure was examined, as shown in Fig. 11(e) and (f). Although some thick twins are sometimes formed, the average twin thickness at 77 K (12.3 nm) is comparable to that (14.9 nm) at room temperature. However, the twin volume fraction is larger at 77 K (15.6%) than at room temperature (10.3%).

We have noticed that DF imaging generally overestimates the thickness and volume fraction of twins (and HCP layers) because information corresponding not only to a Bragg reflection spot but also to streaking within the objective aperture is included in the image. We therefore further investigated evolution of deformation fine microstructures during deformation twinning in the equiatomic Cr-Co-Ni MEA by atomic-resolution STEM imaging using the same thin foils that were used for Fig. 11(a), (c) and (e). Although HCP layers are very difficult to resolve by EBSD mapping in the SEM and TEM DF imaging, thin HCP layers are clearly resolved in the STEM images of Fig. 12(a), (d) and (g) with the incidence of the <110>-type. Histograms of twin and HCP layer thickness distributions are shown in the second and third columns of Fig. 12. Many of the twins are observed to be associated with a thin HCP layer in polycrystals of the equiatomic Cr-Co-Ni MEA (Miao et al., 2017; Niu et al., 2018). The average thickness of thin HCP layers formed next to twins (0.9–1.0 nm; 4–5 atomic layers) does not depend on the strain level at room temperature but it increases to 2.1 nm at 77 K. The increased thickness of HCP layers may reflect the increased phase stability of the HCP structure with respect to the FCC structure at lower temperatures. Some thick HCP layers (2 and 5 nm at room temperature and 77 K, respectively) are sometimes observed to form in isolated form without any association with twins, as shown by the example in Fig. 12(a2). The origin of these thick HCP layers may

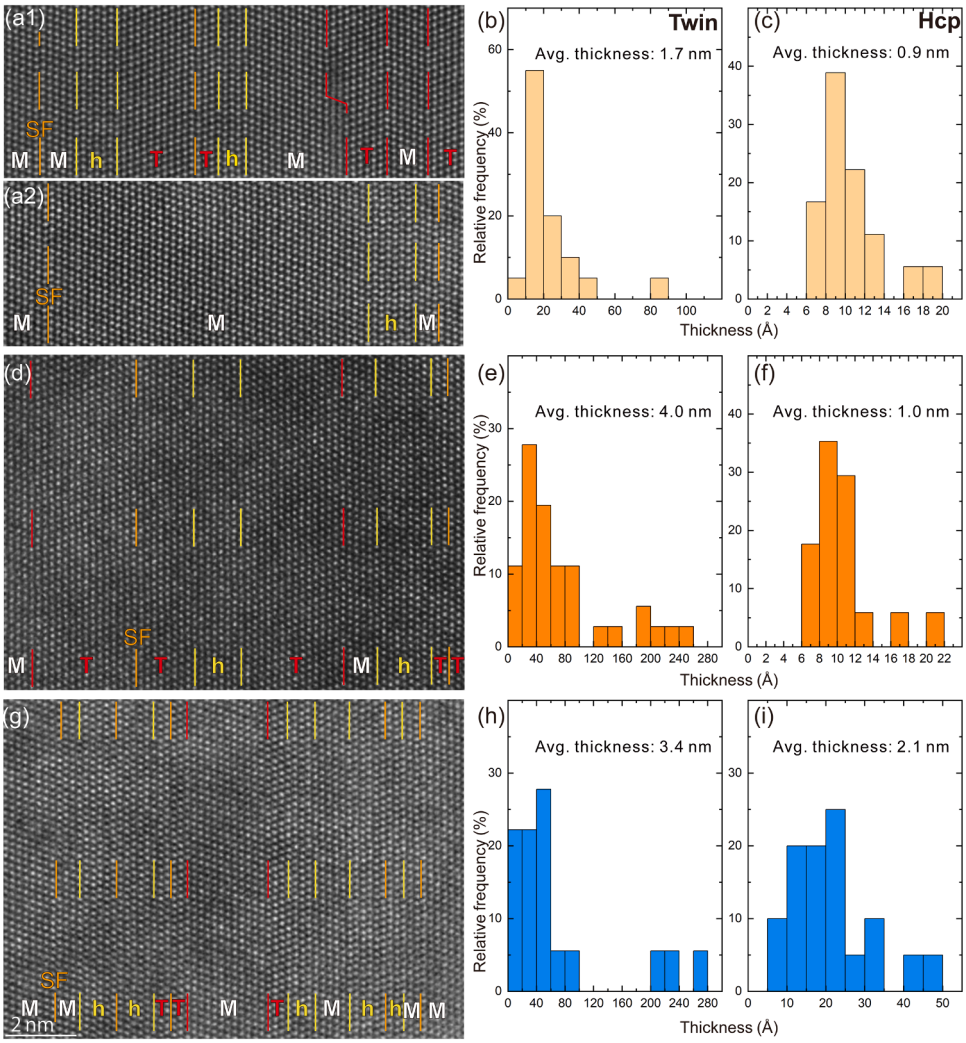

Fig. 12. Atomic-resolution high-angle annular dark-filed (HAADF) STEM images of deformation twins viewed end-on for [$\bar{1}$23]-oriented single crystals of the equiatomic Cr-Co-Ni MEA deformed in tension to different strains: (a) slightly beyond the inflection point, (d) to failure at room temperature and (g) to failure at 77 K. Twin and hcp-layer thickness distributions for (a), (d) and (g) are shown in (b), (e) and (h), and (c), (f) and (i), respectively.

be different from that of thin HCP layers formed next to twins. This will be discussed in detail later in Section 4.2. The occurrence of stacking fault within twins and HCP layers is also clearly resolved, making the twin thickness values estimated by STEM imaging considerably smaller than those estimated by TEM DF imaging although the trend is unchanged. The average twin thickness is observed to increase from 1.7 nm to 4.0 nm as the strain level increases at room temperature, while it is a bit smaller at 77 K (3.4 nm) when compared with the value at failure at room temperature.

4. Discussion

4.1. Slip behavior

The CRSS value obtained in the present study for the {111}<1$\bar{1}$0> slip system in single crystals of the equiatomic Cr-Co-Ni MEA does not depend on the sense of applied stress (tension or compression) and increases with decreasing temperature from 65 ± 5 MPa at room temperature to 133 ± 6 MPa at 77 K. A dulling of the temperature dependence of CRSS, which may be due to the inertia effect occurs below 50 K. If this is ignored, and the temperature dependence of CRSS from above 50 K is extrapolated down to lower temperatures, a CRSS value of 225 MPa is obtained at 0 K. This value is considerably higher than that (168 MPa) obtained by similar extrapolation in the quinary equiatomic Cr-Mn-Fe-Ni-Co HEA (Kawamura et al., 2021), and consistent with predictions of solid-solution hardening from theoretical calculations (Okamoto et al., 2016a; Toda-Caraballo and Rivera-Díaz-del-Castillo, 2015; Varvenne et al., 2017; Zhao and Nieh, 2017), including from MSAD values (Okamoto et al., 2016a).

Solid-solution hardening is considered to be the main hardening mechanism in the present single crystals of the equiatomic Cr-Co-Ni MEA, because the concept of 'stress equivalence' proposed for FCC solid-solution alloys by Basinski et al. (1972) holds true, as shown in Fig. 13(a) and (b). Although the yield strength of the equiatomic Cr-Co-Ni MEA is much higher than those of conventional binary FCC solid solutions, it falls exactly on the extension of the proportionality line between the yield strength at 77 K and the differential yield strength between room temperature and 77 K for a variety of FCC solid solutions (Fig. 13(a)). The values of activation volume measured for the equiatomic Cr-Co-Ni MEA at room temperature and 77 K also fall on their respective master curves together with conventional binary FCC solid solutions if plotted as a function of yield stress (Fig. 13(b)). According to Basinski et al. (1972), such

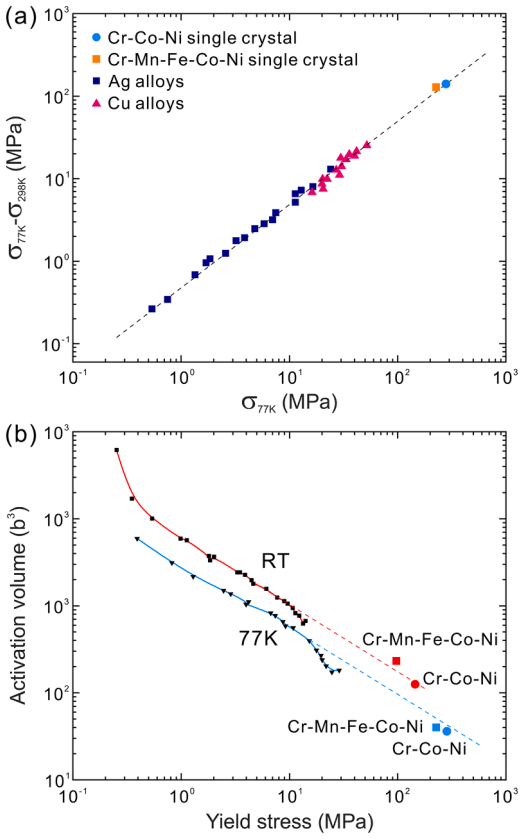

Fig. 13. (a) The difference between the yield strength at 77 K and that at room temperature plotted as a function of the yield strength at 77 K for various FCC solid solutions. The results of Ag alloys and Cu alloys are from Basinski et al. (1972). Axial yield stresses (instead of CRSS) are plotted for the Cr-Co-Ni MEA and Cr-Mn-Fe-Co-Ni HEA (Kawamura et al., 2021) single crystals. (b) Activation volumes at room temperature and 77 K for the Cr-Co-Ni MEA and Cr-Mn-Fe-Co-Ni HEA (Kawamura et al., 2021) single crystals and FCC solid solutions plotted as a function of their yield strength.

trends indicate that the thermal activation process for dislocation glide does not vary from one alloy to another and a single mechanism common to all solid-solution alloys is responsible for the thermal activation process.

In order to check this, we estimate the activation enthalpy for deformation in the present single crystals of the equiatomic Cr-Co-Ni MEA using the results of strain-rate jump tests (Figs. 2 and 5(a)). The shear stress (τ) dependent activation enthalpy, $U(\tau)$ can be calculated from the following equation:

$$\dot{\gamma} = C\exp\left[\frac{-U(\tau)}{kT}\right] \tag{2}$$

where $\dot{\gamma}$, k and T are the same as in Eq. (1) and C is a constant called the reference strain rate of the order of 10^8 s^{-1} (Suzuki and Kuramoto, 1968; Olmsted et al., 2006; Leyson et al., 2010). To eliminate the constant C, we take the logarithm of both sides of Eq. (2) and then differentiate with respect to 1/T,

$$\begin{aligned} U(\tau) &= -k\left[\frac{\partial \ln\dot{\gamma}}{\partial(1/T)}\right]_{\tau} \\ &\approx -k\frac{\ln\dot{\gamma}(\tau, T_2) - \ln\dot{\gamma}(\tau, T_1)}{\frac{1}{T_2} - \frac{1}{T_1}} \end{aligned} \tag{3}$$

Values calculated with Eqs. (2) and (3) are plotted in Fig. 14 with square and circle symbols, respectively. The agreement of the activation enthalpy values calculated with the two equations confirms the validity of choosing C=10^8 s^{-1} in Eq. (2). In contrast, C=10^4 s^{-1} has been assumed in certain theoretical treatments (Olmsted et al., 2006; Leyson et al., 2010; Varvenne et al., 2016, 2017). The activation enthalpy for the equiatomic Cr-Co-Ni MEA is calculated to be 0.61 eV at room temperature. Of interest to note is that the activation enthalpy of conventional FCC solid-solution alloys at room temperature is known to be roughly constant (around 0.6–0.7 eV), regardless of the type of solvent/solute atoms and their concentrations (Suzuki and Kuramoto, 1968). This is further evidence that a single mechanism common to all solid-solution alloys, regardless of whether they are conventional, medium- or high-entropy alloys, is responsible for the thermally activated process of dislocation glide.

4.2. Twinning behavior

The twinning shear stress for conventional FCC alloys is known to increase as stacking fault energy increase while it is believed not to depend much on temperature (Haasen, 1996; Laplanche et al., 2017). Recently, however, Laplanche et al. (2017) reported the opposite trend in polycrystals, namely that the twinning stress is higher for a Cr-Co-Ni MEA than for a Cr-Mn-Fe-Co-Ni HEA despite the former having a lower stacking fault energy. We have found the same opposite trend in [$\bar{1}$23]-oriented single crystals of Cr-Co-Ni (this study) and Cr-Mn-Fe-Co-Ni (Kawamura et al., 2021), as shown Fig. 15(a), which also includes the twinning (shear) stress values obtained from polycrystals of these alloys (Laplanche et al., 2017). The twinning shear stress evaluated at 77 K for single crystals of Cr-Co-Ni (blue circle) and Cr-Mn-Fe-Co-Ni (orange square) are shown in Fig. 15(a) as a function of stacking fault energy. As described in Section 3.2.3, the stacking fault energies plotted likely represent their values at room temperature even though specimens deformed at 77 K were used for the measurement (because partial separation distances were measured in TEM foils at room temperature). For both polycrystals and single crystals, the twinning stress decreases with increasing stacking fault energy, which is opposite to what is generally believed for conventional FCC alloys (Christian and Mahajan, 1995). Additionally, the clear temperature dependence of the twinning shear stress for single crystals of the Cr-Co-Ni MEA shown in Fig. 15(b) is also different from what is generally believed for conventional FCC alloys (Christian and Mahajan, 1995), namely that it should be temperature-independent. Since theoretical

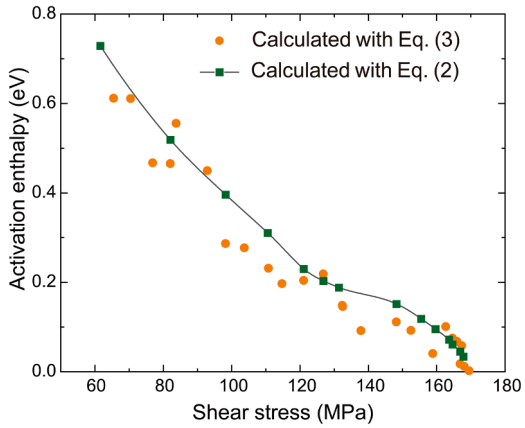

Fig. 14. Shear stress dependence of activation enthalpy for deformation in the equiatomic Cr-Co-Ni MEA calculated using Eq. (2) with C=10^8 s^{-1} and Eq. (3).

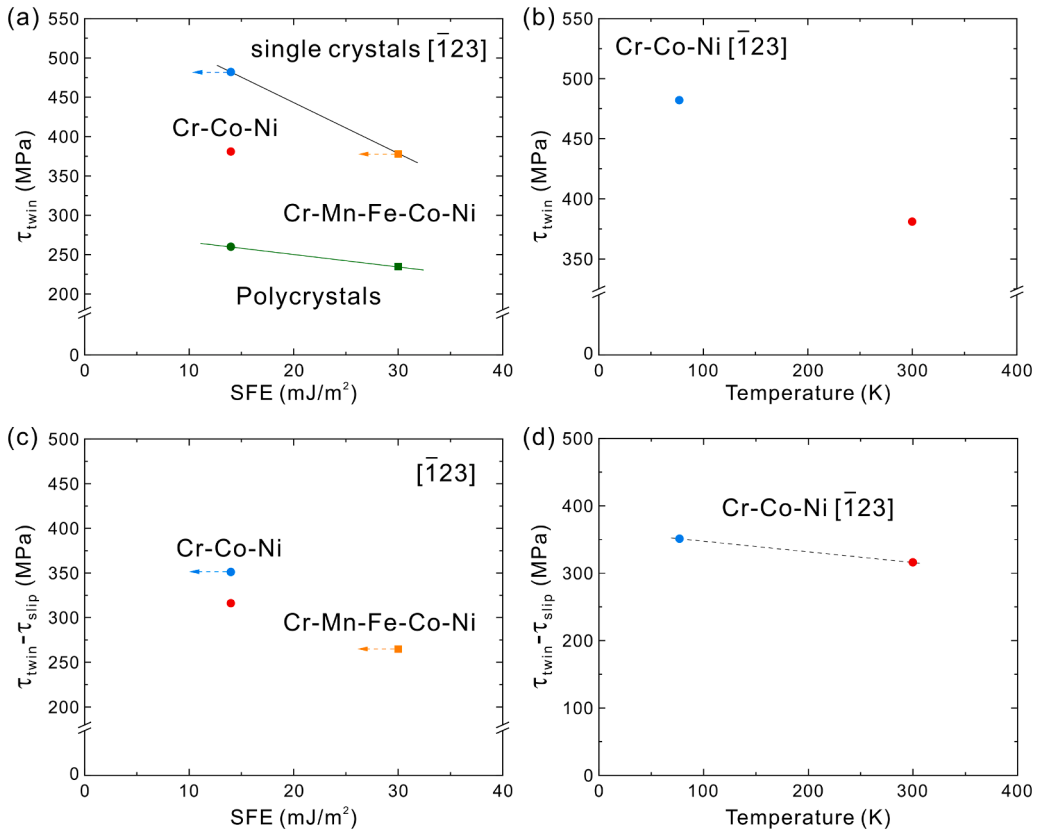

Fig. 15. Dependence of the twinning shear stress for [$\bar{1}$23]-oriented single crystals of the equiatomic Cr-Co-Ni MEA on (a) stacking fault energy and (b) temperature. For comparison, data points for [$\bar{1}$23]-oriented single crystals of the equiatomic Cr-Mn-Fe-Co-Ni HEA (Kawamura et al., 2021) and polycrystals (Laplanche et al., 2017) are also shown. The difference between the twinning shear stress and the CRSS for the (111)[$\bar{1}$01] slip plotted as a function of (c) stacking fault energy and (d) temperature.

calculations indicate that the stacking fault energy of the Cr-Co-Ni MEA decreases with decreasing temperature (Zhang et al., 2017b, 2017c; Zhao et al., 2017), Fig. 15(b) implies that the twinning stress decreases when stacking fault energy increases. As described in Section 3.3, large plastic strain has to be accumulated by slip prior to the commencement of deformation twinning as in the case of TWIP steels (Idrissi et al., 2010a, 2010b, 2013). This causes significantly different twinning shear stress depending on initial crystal orientation. The results of our investigation on the orientation-dependent twinning behavior will be described in follow-on work to add additional perspective to the results in Fig. 15(b). To minimize any effect of the significantly different CRSS values of the Cr-Co-Ni MEA and Cr-Mn-Fe-Co-Ni HEA, the CRSS values were subtracted from the twinning shear stress and the difference plotted in Fig. 15(c) and (d) as a function of stacking fault energy and temperature, respectively. While this difference still exhibits a tendency to decrease with increasing stacking fault energy Fig. 15(c), it is relatively independent of temperature (Fig. 15(d)). The reason for this has yet to be clarified, although the possibility that twinning is indeed stress-dependent cannot be excluded. This will be further investigated with single crystals of other crystal orientations.

Regardless of deformation temperature (room temperature or 77 K), many of the twins are observed to be associated with a thin HCP layer with a thickness of 0.9–1.0 nm and 2.1 nm respectively at room temperature and 77 K. Thin HCP layers associated with twins were also reported by Niu et al. (2018) in polycrystals of the Cr-Co-Ni ternary equiatomic MEA. The average thickness of twins formed is also very small; 4.0 and 3.4 nm, respectively at room temperature and 77 K in the present study. This is consistent with what is observed in conventional FCC alloys. In these conventional FCC alloys, the twin thickness is known to decrease with decrease in stacking fault energy leading to the disappearance of serrations in stress-strain plots as well as clicking sounds during straining as the stacking fault energy decreases (Christian and Mahajan, 1995). Although the reason for this has yet to be clarified in conventional FCC alloys, we suspect a possibility is that the formation of thin HCP layer next to twins limits their thickening and the propensity for HCP layer formation increases with decreasing stacking fault energy (i.e., the stability of the FCC structure decreases relative to the HCP structure). Consequently, formation of HCP layer may be more favored than further twin thickening, as Niu et al. (2018) suggested. This is currently under survey in our research group with molecular dynamic simulations.

In addition to thin HCP layers formed next to twins, some thick HCP layers (2 and 5 nm at room temperature and 77 K, respectively) are sometimes observed to form in isolated form without any association with twins (Fig. 12(a2) and (g)). Although the volume fraction of these isolated HCP layers is much smaller than that of twins, the population of the isolated HCP layers amounts to about

60% of all HCP layers in the early stage of twinning at room temperature and 77 K. This may indicate that the TRIP effect (HCP phase formation) occurs almost concurrently with and at the same stress level as the TWIP effect (twin formation) in the Cr-Co-Ni MEA by the motion of identical Shockley partial dislocations (either on every {111} plane or on every other {111} plane), although the amount of strain carried by the TRIP effect seems not to be large. At room temperature, the population of the isolated HCP layers is reduced to 29% of all HCP layers at failure, indicating the increasing importance of twin thickening in deformation as strain increases.

5. Conclusions

Bulk single crystals of the equiatomic Cr-Co-Ni MEA were tested in compression and tension at temperatures ranging from 14 to 1373 K and their mechanical response correlated with microstructure evolution across multiple length scales. Based on our results, the following conclusions are drawn.

(1) The CRSS for $\{111\}\langle 1\bar{1}0\rangle$ slip at room temperature is 65 ± 5 MPa and it does not depend much on the sense of the applied load (tension or compression). It increases with decrease in temperature from 65 ± 5 MPa at room temperature to 133 ± 6 MPa at 77 K. A dulling of the temperature dependence of CRSS, which may be due to the inertia effect is clearly observed below 50 K. The CRSS at 0 K is estimated to be 225 MPa by extrapolation of the temperature dependence of CRSS from above 50 K to lower temperatures. This value is ~34% higher than the 168 MPa CRSS of the quinary equiatomic Cr-Mn-Fe-Ni-Co HEA obtained using a similar procedure. These values are consistent with theoretical predictions of solid-solution hardening, including those using MSAD values.
(2) The increase in CRSS from room temperature to 77 K implies that the concept of 'stress equivalence' originally proposed for simpler solid solutions holds true also for the equiatomic Cr-Co-Ni MEA except that the CRSS of the present MEA are significantly higher than those of any conventional FCC alloys. Additionally, the activation enthalpy for room-temperature deformation of the equiatomic Cr-Co-Ni MEA is evaluated to be 0.61 eV, which falls within the relatively narrow range (around 0.6–0.7 eV) of conventional FCC alloys, regardless of the type of solvent/solute atoms or their concentrations. This is clear evidence that a single mechanism common to all FCC solid-solution alloys is responsible for the thermal activation process of dislocation glide, regardless of whether they are conventional, medium- or high-entropy alloys.
(3) Dislocations with $1/2\langle 110\rangle$ Burgers vector dissociate into two $1/6\langle 112\rangle$ Shockley partials separated by a wide stacking fault. The stacking fault energy estimated from the separation distance is about 14 mJm^{-2}, which is sufficiently low to account for the planar nature of the observed dislocations and the occurrence of deformation twinning at 77 K and room temperature.
(4) Deformation twinning occurs both at 77 K and room temperature at a high plastic strain, above 150 and 200%, respectively. At 77 K, twinning occurs on conjugate $(\bar{1}\bar{1}1)$ planes in the form of Lüders deformation after the tensile axis overshoots to $[\bar{1}2\ 9\ 21]$ at an onset twinning shear stress of 482 MPa. At room temperature, on the other hand, twinning occurs on primary (111) planes uniformly throughout the gauge section after primary and subsequent conjugate slip at an onset twinning shear stress of 381 MPa. HCP layer formation is observed in association with twinning both at 77 K and room temperature.

CRediT authorship contribution statement

Le Li: Investigation, Data curation, Visualization, Writing – original draft. **Zhenghao Chen:** Investigation. **Shogo Kuroiwa:** Investigation. **Mitsuhiro Ito:** Investigation. **Kyosuke Kishida:** Investigation, Visualization, Writing – review & editing. **Haruyuki Inui:** Supervision, Conceptualization, Methodology, Funding acquisition, Writing – review & editing. **Easo P. George:** Supervision, Writing – review & editing.

Declaration of Competing Interest

The authors declare that they have no known competing financial interests or personal relationships that could have appeared to influence the work reported in this paper.

Acknowledgments

This work was supported by Grant-in-Aids for Scientific Research on innovative Areas on High Entropy Alloys through the grant number JP18H05450 and JP18H05451, in part by JSPS KAKENHI (grant numbers JP18H05478, JP19H00824), the Elements Strategy Initiative for Structural Materials (ESISM) from the Ministry of Education, Culture, Sports, Science and Technology (MEXT) of Japan (grant number JPMXP0112101000), and JST CREST (grant number JPMJCR1994). Structure refinement of the short-range ordering was supplementally corroborated by the synchrotron radiation experiments at the BL02B1 of SPring-8 with the approval of the Japan Synchrotron Radiation Research Institute (JASRI, Proposal Nos. 2018B1321, 2021A1529). EPG is supported by the U.S. Department of Energy, Office of Science, Basic Energy Sciences, Materials Sciences and Engineering Division and acknowledges the JSPS Fellowship for senior scientists that enabled a 2-month stay in HI's group at Kyoto University during which this work was conceived. Dr. K. Niitsu and Mr. K. Ehara of Kyoto University are greatly acknowledged for their help in experiments.

Supplementary materials

Supplementary material associated with this article can be found, in the online version, at doi:10.1016/j.ijplas.2021.103144.

References

Abuzaid, W., Patriarca, L., 2020. A study on slip activation for a coarse-grained and single crystalline CoCrNi medium entropy alloy. Intermetallics 117, 106682. https://doi.org/10.1016/j.intermet.2019.106682.

Bahramyan, M., Mousavian, R.T., Brabazon, D., 2020. Study of the plastic deformation mechanism of TRIP–TWIP high entropy alloys at the atomic level. Int. J. Plast. 127, 102649 https://doi.org/10.1016/j.ijplas.2019.102649.

Basinski, Z.S., Foxall, R.A., Pascual, R., 1972. Stress equivalence of solution hardening. Scr. Metall. 6, 807–814. https://doi.org/10.1016/0036-9748(72)90052-X.

Christian, J.W., Mahajan, S., 1995. Deformation twinning. Prog. Mater. Sci. 1–157. https://doi.org/10.1016/0079-6425(94)00007-7.

Cockayne, D.J.H., Jenkins, M.L., Ray, I.L.F., 1971. The measurement of stacking-fault energies of pure face-centred cubic metals. Philos. Mag. 24, 1383–1392. https://doi.org/10.1080/14786437108217419.

De Cooman, B.C., Estrin, Y., Kim, S.K., 2018. Twinning-induced plasticity (TWIP) steels. Acta Mater. 142, 283–362. https://doi.org/10.1016/j.actamat.2017.06.046.

Ding, J., Yu, Q., Asta, M., Ritchie, R.O., 2018. Tunable stacking fault energies by tailoring local chemical order in CrCoNi medium-entropy alloys. PNAS 115, 8919–8924. https://doi.org/10.1073/pnas.1808660115.

Gali, A., George, E.P., 2013. Tensile properties of high- and medium-entropy alloys. Intermetallics 39, 74–78. https://doi.org/10.1016/j.intermet.2013.03.018.

George, E.P., Raabe, D., Ritchie, R.O., 2019. High-entropy alloys. Nat. Rev. Mater. 4, 515–534. https://doi.org/10.1038/s41578-019-0121-4.

George, E.P., Curtin, W.A., Tasan, C.C., 2020. High entropy alloys: a focused review of mechanical properties and deformation mechanisms. Acta Mater. 188, 435–474. https://doi.org/10.1016/j.actamat.2019.12.015.

Gludovatz, B., Hohenwarter, A., Catoor, D., Chang, E.H., George, E.P., Ritchie, R.O., 2014. A fracture-resistant high-entropy alloy for cryogenic applications. Science 345, 1153–1158. https://doi.org/10.1126/science.1254581.

Gludovatz, B., Hohenwarter, A., Thurston, K.V., Bei, H., Wu, Z., George, E.P., Ritchie, R.O., 2016. Exceptional damage-tolerance of a medium-entropy alloy CrCoNi at cryogenic temperatures. Nat. Commun. 7, 10602. https://doi.org/10.1038/ncomms10602.

Grässel, O., Krüger, L., Frommeyer, G., Meyer, L.W., 2000. High strength Fe–Mn–(Al, Si) TRIP/TWIP steels development — properties — application. Int. J. Plast. 16, 1391–1409. https://doi.org/10.1016/S0749-6419(00)00015-2.

Haasen, P., 1996. Mechanical properties of solid solutions. In: Cahn, R.W., Haasen, P. (Eds.), Physical Metallurgy, 4th ed. North-Holland, Amsterdam, pp. 2009–2073.

Hua, D., Xia, Q., Wang, W., Zhou, Q., Li, S., Qian, D., Shi, J., Wang, H., 2021. Atomistic insights into the deformation mechanism of a CoCrNi medium entropy alloy under nanoindentation. Int. J. Plast. 142, 102997 https://doi.org/10.1016/j.ijplas.2021.102997.

Huang, H., Li, X., Dong, Z., Li, W., Huang, S., Meng, D., Lai, X., Liu, T., Zhu, S., Vitos, L., 2018. Critical stress for twinning nucleation in CrCoNi-based medium and high entropy alloys. Acta Mater. 149, 388–396. https://doi.org/10.1016/j.actamat.2018.02.037.

Idrissi, H., Renard, K., Ryelandt, L., Schryvers, D., Jacques, P.J., 2010a. On the mechanism of twin formation in Fe-Mn-C TWIP steels. Acta Mater. 58, 2464–2476. https://doi.org/10.1016/j.actamat.2009.12.032.

Idrissi, H., Renard, K., Schryvers, D., Jacques, P.J., 2010b. On the relationship between the twin internal structure and the work-hardening rate of TWIP steels. Scr. Mater. 63, 961–964. https://doi.org/10.1016/j.scriptamat.2010.07.016.

Idrissi, H., Renard, K., Schryvers, D., Jacques, P.J., 2013. TEM investigation of the formation mechanism of deformation twins in Fe-Mn-Si-Al TWIP steels. Philos. Mag. 93, 4378–4391. https://doi.org/10.1080/14786435.2013.832837.

Kawamura, M., Asakura, M., Okamoto, N.L., Kishida, K., Inui, H., George, E.P., 2021. Plastic deformation of single crystals of the equiatomic Cr−Mn−Fe−Co−Ni high-entropy alloy in tension and compression from 10K to 1273K. Acta Mater. 203, 116454 https://doi.org/10.1016/j.actamat.2020.10.073.

Laplanche, G., Kostka, A., Horst, O.M., Eggeler, G., George, E.P., 2016. Microstructure evolution and critical stress for twinning in the CrMnFeCoNi high-entropy alloy. Acta Mater. 118, 152–163. https://doi.org/10.1016/j.actamat.2016.07.038.

Laplanche, G., Kostka, A., Reinhart, C., Hunfeld, J., Eggeler, G., George, E.P., 2017. Reasons for the superior mechanical properties of medium-entropy CrCoNi compared to high-entropy CrMnFeCoNi. Acta Mater. 128, 292–303. https://doi.org/10.1016/j.actamat.2017.02.036.

Laplanche, G., Schneider, M., Scholz, F., Frenzel, J., Eggeler, G., Schreuer, J., 2020. Processing of a single-crystalline CrCoNi medium-entropy alloy and evolution of its thermal expansion and elastic stiffness coefficients with temperature. Scr. Mater. 177, 44–48. https://doi.org/10.1016/j.scriptamat.2019.09.020.

Leyson, G.P.M., Curtin, W.A., Hector, L.G., Woodward, C.F., 2010. Quantitative prediction of solute strengthening in aluminium alloys. Nat. Mater. 9, 750–755. https://doi.org/10.1038/nmat2813.

Li, Z., Pradeep, K.G., Deng, Y., Raabe, D., Tasan, C.C., 2016. Metastable high-entropy dual-phase alloys overcome the strength–ductility trade-off. Nature 534, 227–230. https://doi.org/10.1038/nature17981.

Li, Z., Raabe, D., 2017. Strong and ductile non-equiatomic high-entropy alloys: design, processing, microstructure, and mechanical properties. JOM 69, 2099–2106. https://doi.org/10.1007/s11837-017-2540-2.

Li, Z., Zhao, S., Ritchie, R.O., Meyers, M.A., 2019a. Mechanical properties of high-entropy alloys with emphasis on face-centered cubic alloys. Prog. Mater. Sci. 102, 296–345. https://doi.org/10.1016/j.pmatsci.2018.12.003.

Li, Q., Sheng, H., Ma, E., 2019b. Strengthening in multi-principal element alloys with local-chemical-order roughened dislocation pathways. Nat. Commun. 10, 1–11. https://doi.org/10.1038/s41467-019-11464-7.

Liu, S.F., Wu, Y., Wang, H.T., He, J.Y., Liu, J.B., Chen, C.X., Liu, X.J., Wang, H., Lu, Z.P., 2018. Stacking fault energy of face-centered-cubic high entropy alloys. Intermetallics 93, 269–273. https://doi.org/10.1016/j.intermet.2017.10.004.

Lu, X., Zhao, J., Wang, Z., Gan, B., Zhao, J., Kang, G., Zhang, X., 2020. Crystal plasticity finite element analysis of gradient nanostructured TWIP steel. Int. J. Plast. 130, 102703 https://doi.org/10.1016/j.ijplas.2020.102703.

Miao, J., Slone, C.E., Smith, T.M., Niu, C., Bei, H., Ghazisaeidi, M., Pharr, G.M., Mills, M.J., 2017. The evolution of the deformation substructure in a Ni-Co-Cr equiatomic solid solution alloy. Acta Mater. 132, 35–48. https://doi.org/10.1016/j.actamat.2017.04.033.

Miracle, D.B., Senkov, O.N., 2017. A critical review of high entropy alloys and related concepts. Acta Mater. 122, 448–511. https://doi.org/10.1016/j.actamat.2016.08.081.

Niu, C., LaRosa, C.R., Miao, J., Mills, M.J., Ghazisaeidi, M., 2018. Magnetically-driven phase transformation strengthening in high entropy alloys. Nat. Commun. 9, 1363. https://doi.org/10.1038/s41467-018-03846-0.

Okamoto, N.L., Yuge, K., Tanaka, K., Inui, H., George, E.P., 2016a. Atomic displacement in the CrMnFeCoNi high-entropy alloy–a scaling factor to predict solid solution strengthening. AIP Adv. 6, 125008 https://doi.org/10.1063/1.4971371.

Okamoto, N.L., Fujimoto, S., Kambara, Y., Kawamura, M., Chen, Z.M., Matsunoshita, H., Tanaka, K., Inui, H., George, E.P., 2016b. Size effect, critical resolved shear stress, stacking fault energy, and solid solution strengthening in the CrMnFeCoNi high-entropy alloy. Sci. Rep. 6, 35863. https://doi.org/10.1038/srep35863.
Olmsted, D.L., Hector, L.G., Curtin, W.A., 2006. Molecular dynamics study of solute strengthening in Al/Mg alloys. J. Mech. Phys. Solids 54, 1763–1788. https://doi.org/10.1016/j.jmps.2005.12.008.
Otto, F., Yang, Y., Bei, H., George, E.P., 2013a. Relative effects of enthalpy and entropy on the phase stability of equiatomic high-entropy alloys. Acta Mater. 61, 2628–2638. https://doi.org/10.1016/j.actamat.2013.01.042.
Otto, F., Dlouhý, A., Somsen, C., Bei, H., Eggeler, G., George, E.P., 2013b. The influences of temperature and microstructure on the tensile properties of a CoCrFeMnNi high-entropy alloy. Acta Mater. 61, 5743–5755. https://doi.org/10.1016/j.actamat.2013.06.018.
Schneider, M., George, E.P., Manescau, T.J., Záležák, T., Hunfeld, J., Dlouhý, A., Eggler, G., Laplache, G., 2020. Analysis of strengthening due to grain boundaries and annealing twin boundaries in the CrCoNi medium-entropy alloy. Int. J. Plast. 124, 155–169. https://doi.org/10.1016/j.ijplas.2019.08.009.
Schwartz, R.B., Isaac, R.D., Granato, A.V., 1977. Dislocation inertial effects in the plastic deformation of dilute alloys of lead and copper. Phys. Rev. Lett. 38, 554–557. https://doi.org/10.1103/PhysRevLett.38.554.
Shih, M., Miao, J., Mills, M.J., Ghazisaeidi, M., 2021. Stacking fault energy in concentrated alloys. Nat. Commun. 12, 3590. https://doi.org/10.1038/s41467-021-23860-z.
Slone, C.E., Chakraborty, S., Miao, J., George, E.P., Mills, M.J., Niezgoda, S.R., 2018. Influence of deformation induced nanoscale twinning and FCC-HCP transformation on hardening and texture development in medium-entropy CrCoNi alloy. Acta Mater. 158, 38–52. https://doi.org/10.1016/j.actamat.2018.07.028.
Smith, T.M., Hooshmand, M.S., Esser, B.D., Otto, F., McComb, D.W., George, E.P., Ghazisaeidi, M., Mills, M.J., 2016. Atomic-scale characterization and modeling of 60° dislocations in a high-entropy alloy. Acta Mater. 110, 352–363. https://doi.org/10.1016/j.actamat.2016.03.045.
Stobbs, W.M., Sworn, C.H., 1971. The weak beam technique as applied to the determination of the stacking-fault energy of copper. Philos. Mag. 24, 1365–1381. https://doi.org/10.1080/14786437108217418.
Sugita, K., Matsuoka, N., Mizuno, M., Araki, H., 2020. Vacancy formation enthalpy in CoCrFeMnNi high-entropy alloy. Scr. Mater. 176, 32–35. https://doi.org/10.1016/j.scriptamat.2019.09.033.
Suzuki, H., Kuramoto, E., 1968. Thermally activated glide in face-centered cubic alloys. Trans. JIM 9, 697–702 supplement.
Tamm, A., Aabloo, A., Klintenberg, M., Stocks, M., Caro, A., 2015. Atomic-scale properties of Ni-based FCC ternary, and quaternary alloys. Acta Mater. 99, 307–312. https://doi.org/10.1016/j.actamat.2015.08.015.
Tirunilai, A.S., Hanemann, T., Reinhart, C., Tschan, V., Weiss, K.P., Laplanche, G., Freudenberger, J., Heilmaier, M., Kauffmann, A., 2020. Comparison of cryogenic deformation of the concentrated solid solutions CoCrFeMnNi, CoCrNi and CoNi. Mater. Sci. Eng. A 783, 139290. https://doi.org/10.1016/j.msea.2020.139290.
Toda-Caraballo, I., Rivera-Díaz-del-Castillo, P.E., 2015. Modelling solid solution hardening in high entropy alloys. Acta Mater. 85, 14–23. https://doi.org/10.1016/j.actamat.2014.11.014.
Tsai, C.W., Lee, C., Lin, P.O., Xie, X., Chen, S., Carroll, R., LeBlanc, M., Brinkman, B.A.W., Liaw, P.K., Dahmen, K.A., 2019. Portevin-Le Chatelier mechanism in face-centered-cubic metallic alloys from low to high entropy. Int. J. Plast. 122, 212–224. https://doi.org/10.1016/j.ijplas.2019.07.003.
Uzer, B., Picak, S., Liu, J., Jozaghi, T., Canadinc, D., Karaman, I., Chumlyakov, Y.I., Kireeva, I., 2018. On the mechanical response and microstructure evolution of NiCoCr single crystalline medium entropy alloys. Mater. Res. Lett. 6, 442–449. https://doi.org/10.1080/21663831.2018.1478331.
Varvenne, C., Luque, A., Curtin, W.A., 2016. Theory of strengthening in fcc high entropy alloys. Acta Mater. 118, 164–176. https://doi.org/10.1016/j.actamat.2016.07.040.
Varvenne, C., Leyson, G.P.M., Ghazisaeidi, M., Curtin, W.A., 2017. Solute strengthening in random alloys. Acta Mater. 124, 660–683. https://doi.org/10.1016/j.actamat.2016.09.046.
Wu, Y., Bönisch, M., Alkan, S., Abuzaid, W., Sehitoglu, H., 2018. Experimental determination of latent hardening coefficients in FeMnNiCoCr. Int. J. Plast. 105, 239–260. https://doi.org/10.1016/j.ijplas.2018.02.016.
Wu, Z., Bei, H., Otto, F., Pharr, G.M., George, E.P., 2014a. Recovery, recrystallization, grain growth and phase stability of a family of FCC-structured multi-component equiatomic solid solution alloys. Intermetallics 46, 131–140. https://doi.org/10.1016/j.intermet.2013.10.024.
Wu, Z., Bei, H., Pharr, G.M., George, E.P., 2014b. Temperature dependence of the mechanical properties of equiatomic solid solution alloys with face-centered cubic crystal structures. Acta Mater. 81, 428–441. https://doi.org/10.1016/j.actamat.2014.08.026.
Wu, Z., Gao, Y., Bei, H., 2016. Thermal activation mechanisms and Labusch-type strengthening analysis for a family of high-entropy and equiatomic solid-solution alloys. Acta Mater. 120, 108–119. https://doi.org/10.1016/j.actamat.2016.08.047.
Yang, Y., et al., 2021. Bifunctional nanoprecipitates strengthen and ductilize a medium-entropy alloy. Nature 595, 245. https://doi.org/10.1038/s41586-021-03607-y. -240.
Zhang, F.X., Zhao, S., Jin, K., Xue, H., Velisa, G., Bei, H., Huang, R., Ko, J.Y.P., Pagan, D.C., Neuefeind, J.C., Weber, W.J., Zhang, Y., 2017a. Local structure and short-range order in a NiCoCr solid solution alloy. Phys. Rev. Lett. 118, 205501 https://doi.org/10.1103/PhysRevLett.118.205501.
Zhang, Z., Sheng, H., Wang, Z., Gludovatz, B., Zhang, Z., George, E.P., Yu, Q., Mao, S.X., Ritchie, R.O., 2017b. Dislocation mechanisms and 3D twin architectures generate exceptional strength-ductility-toughness combination in CrCoNi medium-entropy alloy. Nat. Commun. 8, 14390. https://doi.org/10.1038/ncomms14390.
Zhang, Y.H., Zhuang, Y., Hu, A., Kai, J., Liu, C.T., 2017c. The origin of negative stacking fault energies and nano-twin formation in face-centered cubic high entropy alloys. Scr. Mater. 130, 96–99. https://doi.org/10.1016/j.scriptamat.2016.11.014.
Zhang, R., Zhao, S., Ding, J., Chong, Y., Jia, T., Ophus, C., Asta, M., Ritchie, R.O., Minor, A.M., 2020. Short-range order and its impact on the CrCoNi medium-entropy alloy. Nature 581, 283–287. https://doi.org/10.1038/s41586-020-2275-z.
Zhao, S., Stocks, G.M., Zhang, Y., 2017. Stacking fault energies of face-centered cubic concentrated solid solution alloys. Acta Mater. 134, 334–345. https://doi.org/10.1016/j.actamat.2017.05.001.
Zhao, Y.Y., Nieh, T.G., 2017. Correlation between lattice distortion and friction stress in Ni-based equiatomic alloys. Intermetallics 86, 45–50. https://doi.org/10.1016/j.intermet.2017.03.011.
Zhou, D., Chen, Z., Ehara, K., Niitsu, K., Tanaka, K., Inui, H., 2020. Effects of annealing on hardness, yield strength and dislocation structure in single crystals of the equiatomic Cr-Mn-Fe-Co-Ni high entropy alloy. Scr. Mater. 191, 173–178. https://doi.org/10.1016/j.scriptamat.2020.09.039.